Nanoscale

COMMUNICATION

View Article Online
View Journal | View Issue

Cite this: *Nanoscale*, 2018, **10**, 12963

Received 12th May 2018,
Accepted 27th June 2018

DOI: 10.1039/c8nr03840f

rsc.li/nanoscale

Porous $CaFe_2O_4$ as a promising lithium ion battery anode: a trade-off between high capacity and long-term stability†

Chunhua Han,* Xiao Zhang, Xiaoming Xu, Qi Li, Qiu He, Jiashen Meng, Xuanpeng Wang, Ziang Liu, Peijie Wu and Liqiang Mai *

Metal oxides are considered as attractive candidates as anode materials for lithium ion batteries (LIBs) due to their high capacities compared to commercialized graphite. However, fast capacity fading, which is caused by inherent large volume expansions and agglomeration of active particles upon cycling, is a great challenge. Herein, we propose the design of porous $CaFe_2O_4$ electrode material to address the above issue. Compared to pristine iron oxides, $CaFe_2O_4$ exhibits a distinct trade-off in terms of high capacity and long-term stability, which is beneficial to the potential practical applications. Such a trade-off effect is attributed to the synergistic effect between the porous structure and the *in situ* formed CaO nanograins during charging/discharging processes. This work provides an effective strategy in achieving anode materials with high capacity and long-term stability for next-generation LIBs.

Introduction

Lithium ion batteries (LIBs) have been the power source for mobile electronic devices, owing to their high energy density, high output voltage and long lifespan.[1–4] In recent years, LIBs have also been regarded as the main technological route for electric vehicles. As the endurance mileage requirement of electric vehicles is increasing, it is urgent for researchers to develop LIBs with higher energy density and longer cycle life. The energy density of the battery depends on the voltage gradient between the negative and positive electrodes and the specific capacities of the materials.[5] Therefore, extensive researches are devoted to the development of high-voltage cathode materials or high-capacity anode materials.[6] Graphite, as a commercial anode material, is no longer enough to meet the demand for the development of electric vehicles owing to the lower capacity (372 mA h g^{-1}). Alternatively, metal oxide anodes have attracted considerable attention in the past years owing to their high theoretical capacity.[7–11] Among them, iron based materials, such as Fe_2O_3 and Fe_3O_4, have already been the focus of many studies owing to their abundant resource, high specific capacities, environmental benignity and low preparation cost.[12–31] However, the inevitable volume change during charging and discharging causes the pulverization of electrode materials and further the detachment from the current collectors, thus leading to the rapid decay of capacity.

To date, extensive efforts have been devoted to pursuing high-performance Fe-based anodes, for instance by carbon coating,[13–17] graphene oxide decoration[18–22] and complex nanostructure design.[23–31] Although these strategies have resolved some major problems and immensely extended the cycle life, other new issues still exist. For example, nanomaterials with the presence of nano-carbon coating will reduce the tap density of the materials; the high cost of graphene cannot be ignored for graphene decoration; and those strategies of complex nanostructure design generally involve multiple steps, leading to high fabrication cost and low yield.

The introduction of inactive components (CaO, MgO, SrO) into electroactive metal oxides is also an effective strategy for improving the electrochemical performance of high-capacity metal oxide anodes.[32–34] Among them, Ca-containing compounds show improved rate capability and cycling stability, which benefit from the *in situ* formation of CaO during charge/discharge processes, such as $Ca_3Co_4O_9$ nanoplates,[32] $CaSnO_3$ nanotube,[35] $Ca_2Ge_7O_{16}$ nanowires[36] and CaV_4O_9 nanowires.[34] Compared to other Ca-containing compounds, $CaFe_2O_4$ has tremendous potential considering its natural abundance, environmental benignity and nontoxicity. In previous reports, $CaFe_2O_4$ was mainly studied in view of its excellent magnetic, optical and catalytic properties.[37–40] Although the lithium storage activity of $CaFe_2O_4$ has been previously reported,[41] the comprehensive investigation of $CaFe_2O_4$ anode with excellent electrochemical performance is still rarely studied. Compared with graphite, Fe_2O_3 and silicon, $CaFe_2O_4$ has many intriguing properties when used as LIB anode (Table S1†). In terms of

State Key Laboratory of Advanced Technology for Materials Synthesis and Processing, International School of Materials Science and Engineering, Wuhan University of Technology, Luoshi Road 122, Wuhan, 430070 Hubei, China.
E-mail: hch5927@whut.edu.cn, mlq518@whut.edu.cn

† Electronic supplementary information (ESI) available: XRD, SEM, TG, electrochemical properties. See DOI: 10.1039/c8nr03840f

capacity, the theoretical capacity (770 mA h g^{-1}) of $CaFe_2O_4$ is approximately two times of that of commercial graphite. Compared with Fe_2O_3 and silicon, the volume expansion of $CaFe_2O_4$ during cycling is not so serious. Besides, the density of $CaFe_2O_4$ is much higher than that of graphite and silicon, suggesting a potentially higher volumetric capacity. In light of these properties, $CaFe_2O_4$ is expected to show a distinct trade-off between high capacity and long-term stability.

Herein, we prepared porous $CaFe_2O_4$ through a simple sol–gel approach combined with subsequent calcination process in air. When tested as an anode material in LIBs, porous $CaFe_2O_4$ exhibits a distinct trade-off between high capacity and long-term stability in comparison to pristine Fe_2O_3. The obtained $CaFe_2O_4$ provides a high discharge capacity of 816 mA h g^{-1} at a specific current of 0.1 A g^{-1}. A discharge capacity of 532 mA h g^{-1} after 1000 cycles was achieved at 0.5 A g^{-1}, with an average capacity fading of 0.013% per cycle. Furthermore, stable cycling of electrode at a high mass loading of 3.93 mg cm^{-2} with a high areal capacity of 2.32 mA h cm^{-2} was realized. The CaO nanograins are demonstrated to be formed as a dispersant during the charging/discharging process, which can alleviate the mechanical stress induced by the volume expansion and prevent the aggregation of the active nanograins upon cycling, leading to the increased long-term stability. The electrode manifests both high capacity and ultra-long cycling performance, showing great potential as an anode material for the high-performance LIBs.

Experimental

Synthesis of the porous $CaFe_2O_4$, Fe_2O_3, $MgFe_2O_4$

For a typical synthesis, the porous $CaFe_2O_4$ was prepared through a simple sol–gel approach followed by heat treatment. First, 2 g of Polyvinylpyrrolidone (PVP, average M_w = 1 300 000) was dissolved in 25 ml of *N*,*N*-dimethylformamide (DMF, anhydrous, 99.8%) solvent, which was magnetic stirred vigorously for 1 h at room temperature. Then, 4 mmol of calcium nitrate tetrahydrate ($Ca(NO_3)_2{\cdot}4H_2O$, 99%) and 8 mmol of iron(III) nitrate nonahydrate ($Fe(NO_3)_3{\cdot}9H_2O$, 99%) were dissolved in PVP-DMF solution (PVP acts as a dispersant, which makes the solution viscous and uniform. DMF acts as a solvent) with vigorous stirring at room temperature for another 2 h until solution turned to oxblood red. Then, the sample was placed in an oven at 70 °C overnight. The dried mixture by the previous step was firstly stabilized in muffle furnace at 250 °C for 1 h. Then, the temperature was increased to 800 °C and held for 5 h. The heating rate of the muffle furnace is 5 °C min^{-1}. For comparison, Fe_2O_3 bulk was also synthesized under the same condition without $Ca(NO_3)_2{\cdot}4H_2O$. $MgFe_2O_4$ bulk was synthesized using the same synthesis procedures mentioned above except that $Ca(NO_3)_2{\cdot}4H_2O$ was replaced by $Mg(NO_3)_2{\cdot}6H_2O$.

Material characterization

X-ray diffraction (XRD) was performed to characterize the crystallographic information of the samples using Burker D8 Discover X-ray diffractometer with Cu-Kα radiation (λ = 1.5418 Å). Scanning electron microscopic (SEM) data and energy dispersive X-ray spectra (EDS) were collected with a JEOL-7100F SEM/EDS microscope at an acceleration voltage of 20 kV. The morphology of the product was examined by transmission electron microscopic (TEM) and high resolution transmission electron microscopic (HRTEM) with a JEOL JEM-2100 F STEM/EDS microscope. Thermogravimetric analysis (TGA) was performed using a Netzsch STA 449C with a heating rate of 10 °C min^{-1} under air.

Electrochemical measurements

The electrochemical evaluation was performed by assembling 2016 coin-type cells in a glove box filled with highly pure argon atmosphere. The active materials, carbon black and sodium carboxyl methyl cellulose (CMC) were mixed in the ratio 7 : 2 : 1 using water. The copper foil coated with active materials was dried at 70 °C for 12 h. The loading content of the active materials on copper foil was about 0.5 to 4.0 mg cm^{-2}. 1 M $LiPF_6$ in ethylene carbonate (EC), dimethyl carbonate (DMC) and ethylene methyl carbonate (EMC) (1 : 1 : 1, in volume) was used as the electrolyte. And a polypropylene film (Celgard-2300) was used as the separator. The assembled coin cells were placed for 12 hours at room temperature before the electrochemical tests to ensure that the electrolyte was completely immersed in the electrode materials. The LAND CT2001A multichannel galvanostat (Wuhan, China) was used to perform galvanostatic discharge/charge tests in the voltage window of 0.01–3.0 V (*vs.* Li^+/Li). Cyclic voltammetry (CV) was conducted on an Autolab potentiostat/galvanostat. CV curves were recorded in the potential window of 0.01–3.0 V at a scan rate of 0.1 mV s^{-1}. EIS spectra were collected by applying sine wave perturbation voltage with an amplitude of 5 mV over the frequency range 100 kHz to 0.01 Hz.

Results and discussion

The synthetic process for the fabrication of the porous $CaFe_2O_4$ is shown in Scheme 1. In the first step, all the chemicals were uniformly dissolved in the solution. Then, the solu-

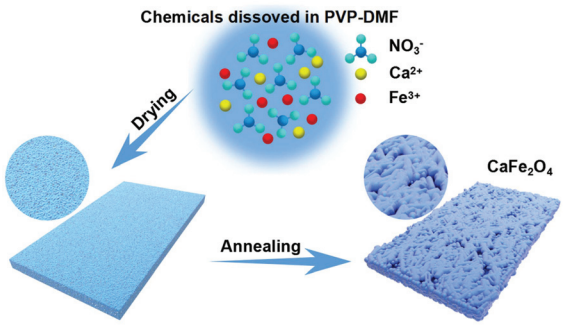

Scheme 1 Schematic illustration of the formation procedure of porous $CaFe_2O_4$.

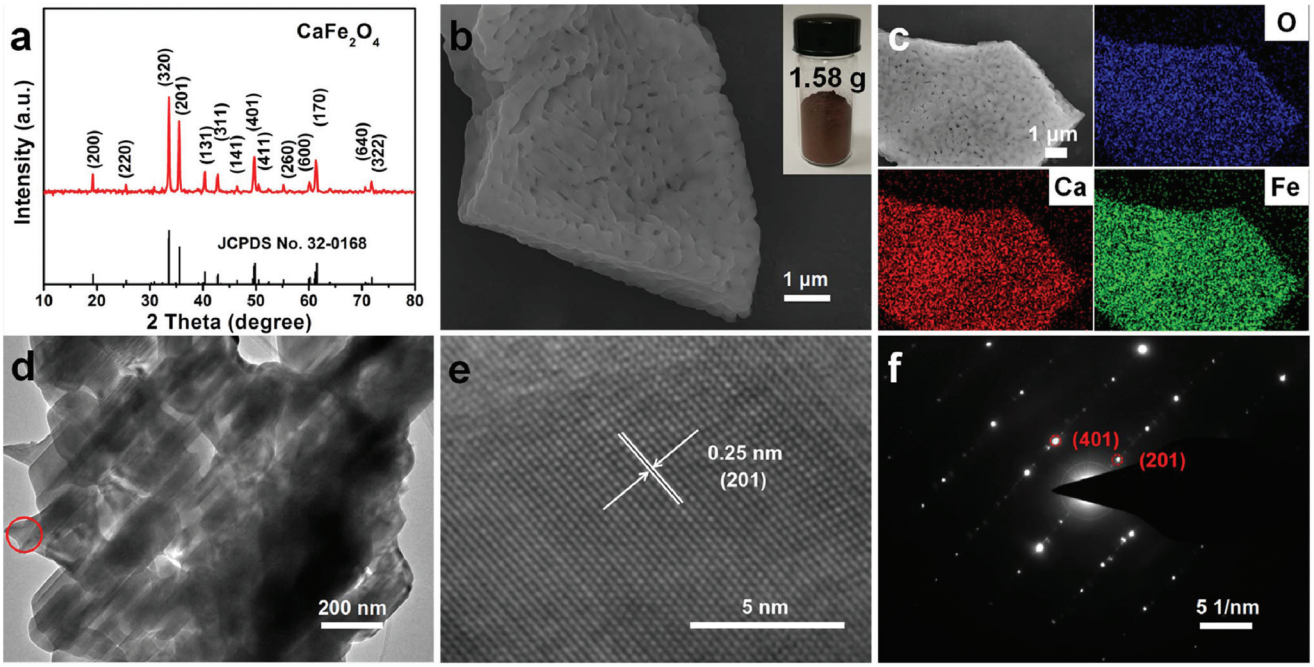

Fig. 1 (a) XRD pattern, (b) SEM image, (c) the corresponding elemental mapping, (d) TEM image, (e) HRTEM image, and (f) SAED pattern of porous $CaFe_2O_4$. The inset image in (b) shows the optical photo of the obtained $CaFe_2O_4$ material.

tion was dried to form the precursor. After the subsequent heat treatment process in air, $CaFe_2O_4$ was obtained. During the annealing process, the decomposition of $Ca(NO_3)_2{\cdot}4H_2O$ resulted in the generation of large pores in the obtained $CaFe_2O_4$.

The XRD pattern of the final product after sintering at 800 °C is shown in Fig. 1a, revealing that it was orthorhombic $CaFe_2O_4$ (JCPDS no. 32-0168). Low-magnification SEM image of the final sample displays the bulk morphology with the edge length of ~10 μm (Fig. 1b). EDS mappings reveal the existence and uniform distribution of Ca, Fe, O elements (Fig. 1c). According to the SEM images and TEM image (Fig. 1d), a number of voids can be observed clearly, exhibiting a porous structure. The HRTEM image (Fig. 1e) shows clear lattice fringes (d = 0.25 nm), which matches well with the (201) plane of $CaFe_2O_4$ crystal. The SAED pattern (Fig. 1f) further verifies the good crystalline nature of the as-synthesized $CaFe_2O_4$. In addition, the inset image in Fig. 1b is 1.58 g of the final product produced at lab scale.

Meanwhile, the XRD patterns of the as-prepared product calcined at series of temperatures are displayed in Fig. S1.† It was found that the sample annealed at 600 °C showed an approximately amorphous state. When the temperature increased to above 700 °C, the sample was found to crystallize into a defined $CaFe_2O_4$ phase. The morphology evolution of $CaFe_2O_4$ samples calcined at different temperatures was also investigated (Fig. S2†). It was found that the sample annealed at 600 °C displayed dense bulks with a smooth surface, while annealed at 700 °C, large amounts of small pores were found. With the increase of annealing temperature to 800 °C, larger pores can be easily observed on the bulk structure (Fig. S2†). For comparison, both Fe_2O_3 and $MgFe_2O_4$ with highly crystalline structure (Fig. S3†) were synthesized using similar method but interestingly, they do not show any obvious voids in the bulk (Fig. S4†). To reveal what makes the morphology differences between Fe_2O_3, $MgFe_2O_4$ and $CaFe_2O_4$, TGA of $Ca(NO_3)_2{\cdot}4H_2O$ and $Mg(NO_3)_2{\cdot}6H_2O$ was carried out under air atmosphere. As shown in Fig. S5a,† there were two significant endothermic peaks in the DSC curve in the range of 550–660 °C for calcium nitrate, together with a significant mass loss as shown in the TG curve, indicating the decomposition of $Ca(NO_3)_2$. However, the decomposition of $Mg(NO_3)_2$ was observed in the range of 400–450 °C (Fig. S5b†). Therefore, it is proposed that the release of gas produced by decomposition of $Ca(NO_3)_2$ results in the generation of observed pores in $CaFe_2O_4$ bulks. As for $MgFe_2O_4$, it is speculated that the porous structure was produced in the early stage due to the lower decomposition temperature of $Mg(NO_3)_2$, but the pores closed during the higher annealing process.

Cyclic voltammetry (CV) of the $CaFe_2O_4$ electrode for the first three cycles (Fig. 2a) was carried out. The distinct differences are observed in the cathodic peak between 1st and 2nd discharge, which can be attributed to the irreversible conversion reaction in the initial discharge process, as observed in most other metal–oxide anodes. The peak at ~0.52 V observed in the first cathodic sweep is associated with the reduction of Fe^{3+}, the generation of CaO as well as the irreversible formation of the solid electrolyte interphase (SEI) film.[41–46] In the anodic sweep process, a broad oxidation peak at ~1.5 V can be associated with a reversible oxidation reaction of Fe.

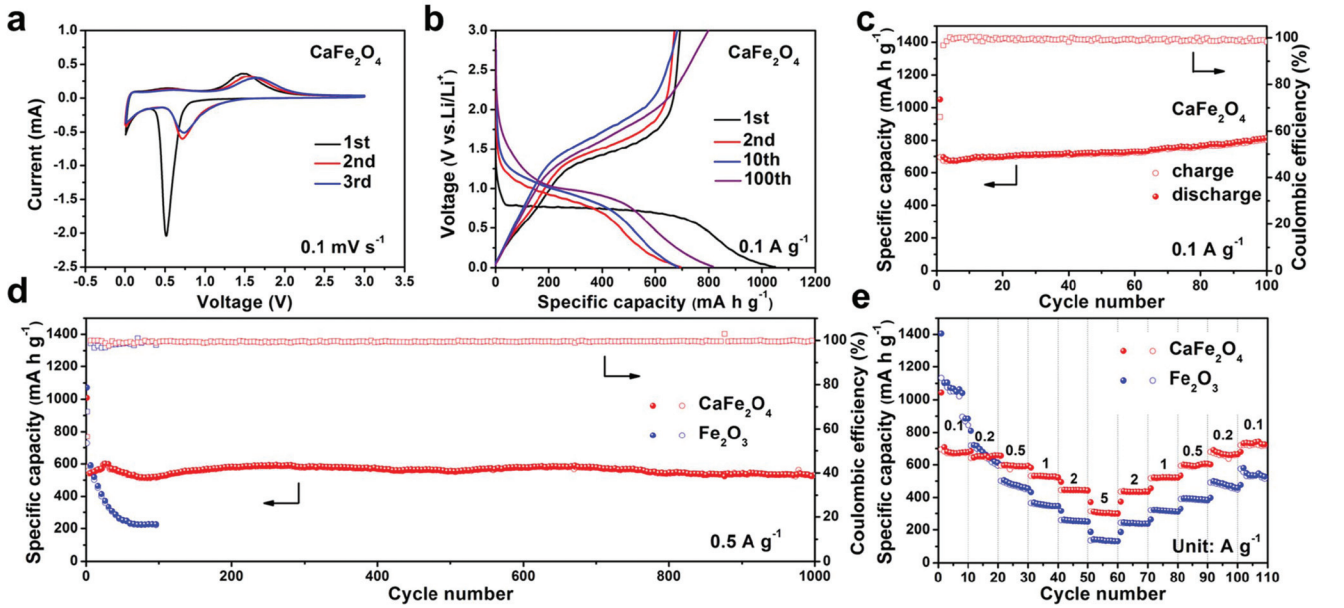

Fig. 2 Electrochemical performances of the half cells with the porous $CaFe_2O_4$ and the Fe_2O_3 bulk as the anodes: (a) CV curves of the first three cycles at a scan rate of 0.1 mV s^{-1}, (b) charge/discharge curves at the current density of 0.1 A g^{-1} (c) cycling performance at the current density of 0.1 A g^{-1} of $CaFe_2O_4$ electrode; (d) cycling performances at the current density of 0.5 A g^{-1}, and (e) rate performances of $CaFe_2O_4$ electrode and Fe_2O_3 electrode.

Additionally, the curves after the first cycle almost overlap, indicating the highly reversible conversion in the following cycling processes.

The charge/discharge profiles (Fig. 2b) of the porous $CaFe_2O_4$ are displayed at 0.1 A g^{-1}. The porous $CaFe_2O_4$ delivers initial discharge and charge specific capacities of 1050 and 695.4 mA h g^{-1}, respectively, corresponding to an initial coulombic efficiency (ICE) of 66%. The observed irreversible capacity loss can be ascribed to the formation of SEI layer and the irreversible Li trapping in the structure.[47,48]

Fig. 2c displays the cycling performance of porous $CaFe_2O_4$ at 0.1 A g^{-1}. The capacity of the porous $CaFe_2O_4$ was found to increase gradually from 695 mA h g^{-1} at the 2nd cycle to 816 mA h g^{-1} at 100th cycles. This gradual increase in capacity commonly occurs in various transition metal oxides.[19,49–52] Such a behavior is normally attributed to the activation of the electrode materials and the growth of a polymer/gel-like film.[51,53] Stability upon cycling for 1000 cycles at 0.5 A g^{-1} with the high capacity retention is shown in Fig. 2d. The second discharge capacity is 611 mA h g^{-1} and a discharge capacity of 532 mA h g^{-1} is remained after 1000 cycles, reaching a capacity retention of 87%. In comparison, Fe_2O_3 electrode suffers from a drastic capacity degradation, with a low capacity retention of only 32%. Fig. S6† shows that porous $CaFe_2O_4$ still owns a discharge capacity of 404 mA h g^{-1} after 900 cycles with the capacity retention of 80% at 1 A g^{-1}.

Fig. 2e shows the rate capabilities of porous $CaFe_2O_4$ and Fe_2O_3 bulk at various current densities. The porous $CaFe_2O_4$ displays a better rate capability and exhibits high reversible capacities of 679, 652, 593, 526, 439 and 311 mA h g^{-1} at 0.1, 0.2, 0.5, 1.0, 2.0 and 5.0 A g^{-1}, respectively. Besides, the capacity recovers to 733 mA h g^{-1} as the current density reduces back to 0.1 A g^{-1}, revealing the good reversibility and stability of the materials. As a comparison, the Fe_2O_3 bulk shows much lower capacity of 154 mA h g^{-1} at 5 A g^{-1}. When the current density returns back to 0.1 A g^{-1} gradually, the Fe_2O_3 bulk shows significant capacity decay with a retention of 47% only. The electrochemical impedance spectroscopy (EIS) results of $CaFe_2O_4$ and Fe_2O_3 after five cycles are shown in Fig. S7.† The charge transfer resistance (R_{ct}) of $CaFe_2O_4$ is lower than that of Fe_2O_3, indicating $CaFe_2O_4$ has a faster charge transfer process for Li-ion insertion and extraction.

To further demonstrate the superior electrochemical stability of porous $CaFe_2O_4$, cycling performances at different mass loadings were tested (Fig. 3a). The porous $CaFe_2O_4$ active material with the mass loadings of 0.99, 1.94 and 3.93 mg cm^{-2} delivered areal capacities of 0.55, 1.22 and 2.32 mA h cm^{-2}, respectively. It is worth noting that the significant increase of mass loading leads to slight decrease in gravimetric capacity but distinct increase in areal capacity (Fig. 3b). To the best of

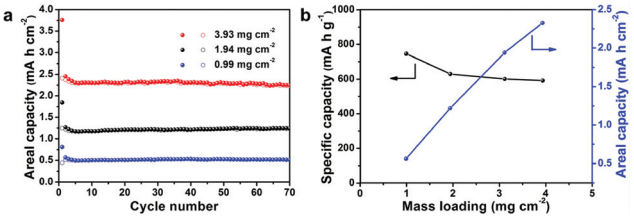

Fig. 3 (a) Cycling performance and (b) specific gravimetric and areal capacities of the porous $CaFe_2O_4$ anode at different mass loadings.

our knowledge, the high areal capacity (2.32 mA h cm^{-2}) with a stable cycling at such a high mass loading (3.93 mg cm^{-2}) obtained here was rarely reported for Fe-based anode materials in previous studies.[25,54–60]

To reveal the Li storage mechanism of porous $CaFe_2O_4$, *ex situ* TEM analyses were also performed. It can be found that intact micron-scale bulk with the porous structure of $CaFe_2O_4$ was maintained at the fully discharged state after five cycles (Fig. 4a). From the SAED pattern (Fig. 4b), the diffraction spots in the green circle correspond to a spacing of 0.13 nm, confirming the generation of CaO (JCPDS no. 01-1160). The diffraction spots with the spacings of 0.15 and 0.25 nm can be indexed to the (440) plane of $Li_2Fe_3O_4$ (JCPDS no. 37-1432) and the (311) plane of $Li_{0.64}Fe_{5.36}O_8$ (JCPDS no. 70-2709), indicating the existence of Li-intercalated phases.[47,61,62] The TEM image and SAED pattern of $CaFe_2O_4$ at the fully charged state after five cycles are also shown in Fig. S8.† The porous structure of $CaFe_2O_4$ shows no obvious change after five cycles. The typical diffraction spots of CaO, Fe_2O_3 (JCPDS no. 33-0664), Fe_3O_4 (JCPDS no. 02-1035) are detected in the SAED pattern. As shown in the TEM image of the $CaFe_2O_4$ at the lithiation state after 300 cycles, the morphology retains its integrity (Fig. 4c). The typical diffraction rings of CaO and Fe (JCPDS no. 87-0722) are both detected in the SAED pattern (Fig. 4d). No diffraction rings of Li_2O are observed, revealing the amorphous state. The lithium storage mechanism of the $CaFe_2O_4$ upon discharge process is further investigated by *in situ* XRD (Fig. S9†). In the first discharge process, the peaks centered at 33.6° and 35.5° weaken, indicating the consumption of pristine $CaFe_2O_4$ and the amorphization of the structure. The above analyses indicate a typical conversion reaction mechanism of $CaFe_2O_4$ for Li storage with the generation of CaO, but in initial cycles there seems to be an activation process with the formation of intermediate phases of Li–Fe–O.

Based on the above results, we can conclude that the introduction of Ca element to Fe_2O_3 results in a decreased specific capacity because of the inert electrochemical property of Ca. However, the *in situ* generated CaO nanograins can effectively buffer the volume expansion and inhibit the agglomeration of active material nanoparticles and thus greatly promote the cycling stability. We believe such a trade-off effect between high capacity and long-term stability is highly significant for the potential practical applications.

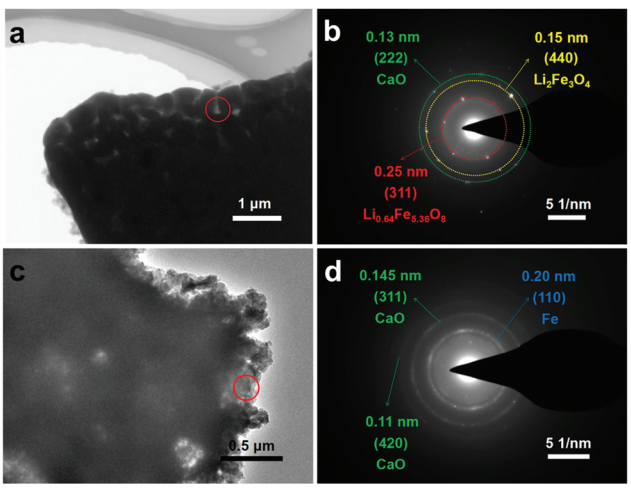

Fig. 4 (a, c) TEM images, (b, d) SAED patterns of $CaFe_2O_4$ at the lithiation state at 0.5 A g^{-1} after 5 cycles and 300 cycles, respectively.

Conclusions

In summary, the porous $CaFe_2O_4$ has been synthesized through a facile sol–gel method successfully. When used as a LIB anode material, the porous $CaFe_2O_4$ exhibits promising performances including relatively high capacity (a capacity of 816 mA h g^{-1} at 0.1 A g^{-1}) and ultrastable cycling stability (a capacity retention of 87% at 0.5 A g^{-1} after 1000 cycles and a capacity retention of 80% at 1 A g^{-1} after 900 cycles). A high areal capacity of 2.3 mA h cm^{-2} with stable cycling at the mass loading of 3.93 mg cm^{-2} is achieved. During charging and discharging of $CaFe_2O_4$, the CaO nanograins can be *in situ* generated, which can prevent agglomeration of active particles. All these results demonstrate that the incorporation of the inactive components can effectively improve the cycling stability, showing a relative balance between high capacity and long-term stability. Considering the simple fabrication and impressive electrochemical performance of porous $CaFe_2O_4$, this research may pave the way for developing high capacity and long-term stable anode materials for next-generation LIBs.

Conflicts of interest

There are no conflicts to declare.

Acknowledgements

This work was supported by the National Natural Science Fund for Distinguished Young Scholars (51425204), the National Natural Science Foundation of China (51521001), the National Key Research and Development Program of China (2016YFA0202603), the Programme of Introducing Talents of Discipline to Universities (B17034), the Yellow Crane Talent (Science & Technology) Program of Wuhan City, the International Science & Technology Cooperation Program of China (2013DFA50840) and the Fundamental Research Funds for the Central Universities (WUT: 2016III001, 2017III009).

Notes and references

1 L. Ji, Z. Lin, M. Alcoutlabi and X. Zhang, *Energy Environ. Sci.*, 2011, **4**, 2682–2699.
2 B. Dunn, H. Kamath and J.-M. Tarascon, *Science*, 2011, **334**, 928–935.
3 J. M. Tarascon and M. Armand, *Nature*, 2001, **414**, 359–367.

4 L. Mai, M. Yan and Y. Zhao, *Nature*, 2017, **546**, 469–470.
5 M. Armand and J. M. Tarascon, *Nature*, 2008, **451**, 652–657.
6 Z. Xiao, J. Meng, Q. Li, X. Wang, M. Huang, Z. Liu, C. Han and L. Mai, *Sci. Bull.*, 2018, **63**, 46–53.
7 V. Raju, X. Wang, W. Luo and X. Ji, *Chem. – Eur. J.*, 2014, **20**, 7686–7691.
8 D. Liu, B. B. Garcia, Q. Zhang, Q. Guo, Y. Zhang, S. Sepehri and G. Cao, *Adv. Funct. Mater.*, 2009, **19**, 1015–1023.
9 K. Zhao, M. Wen, Y. Dong, L. Zhang, M. Yan, W. Xu, C. Niu, L. Zhou, Q. Wei and W. Ren, *Adv. Energy Mater.*, 2017, **7**, 1601582.
10 L. Zhang, P. Hu, X. Zhao, R. Tian, R. Zou and D. Xia, *J. Mater. Chem.*, 2011, **21**, 18279–18283.
11 Y. Huang, X.-L. Huang, J.-S. Lian, D. Xu, L.-M. Wang and X.-B. Zhang, *J. Mater. Chem.*, 2012, **22**, 2844–2847.
12 L. Zhang, H. B. Wu and X. W. Lou, *Adv. Energy Mater.*, 2014, **4**, 1300958.
13 W. M. Zhang, X. L. Wu, J. S. Hu, Y. G. Guo and L. J. Wan, *Adv. Funct. Mater.*, 2010, **18**, 3941–3946.
14 N. Zhang, X. Han, Y. Liu, X. Hu, Q. Zhao and J. Chen, *Adv. Energy Mater.*, 2015, **5**, 1401123.
15 C. He, S. Wu, N. Zhao, C. Shi, E. Liu and J. Li, *ACS Nano*, 2013, **7**, 4459–4469.
16 X. Li, Y. Ma, G. Cao and Y. Qu, *J. Mater. Chem. A*, 2016, **4**, 12487–12496.
17 W. Zhang, X. Li, J. Liang, K. Tang, Y. Zhu and Y. Qian, *Nanoscale*, 2016, **8**, 4733–4741.
18 T. Jiang, F. Bu, X. Feng, I. Shakir, G. Hao and Y. Xu, *ACS Nano*, 2017, **11**, 5140–5147.
19 G. Zhou, D. W. Wang, F. Li, L. Zhang, N. Li, Z. S. Wu, L. Wen, G. Q. Lu and H. M. Cheng, *Chem. Mater.*, 2010, **22**, 5306–5313.
20 J. Ma, Y.-S. He, W. Zhang, J. Wang, X. Yang, X.-Z. Liao and Z.-F. Ma, *Nano Energy*, 2015, **16**, 235–246.
21 G.-W. Zhou, J. Wang, P. Gao, X. Yang, Y.-S. He, X.-Z. Liao, J. Yang and Z.-F. Ma, *Ind. Eng. Chem. Res.*, 2012, **52**, 1197–1204.
22 L. Zhuo, Y. Wu, L. Wang, J. Ming, Y. Yu, X. Zhang and F. Zhao, *J. Mater. Chem. A*, 2013, **1**, 3954–3960.
23 Z. Na, G. Huang, F. Liang, D. Yin and L. Wang, *Chem. – Eur. J.*, 2016, **22**, 12081–12087.
24 D. Li, K. L. Wang, H. W. Tao, X. H. Hu, S. J. Cheng and K. Jiang, *RSC Adv.*, 2016, **6**, 89715–89720.
25 F. X. Ma, H. Hu, H. B. Wu, C. Y. Xu, Z. Xu and L. Zhen, *Adv. Mater.*, 2015, **27**, 4097–4101.
26 B. Wang, J. S. Chen, H. B. Wu, Z. Wang and X. W. Lou, *J. Am. Chem. Soc.*, 2011, **133**, 17146–17148.
27 Q. An, F. Lv, Q. Liu, C. Han, K. Zhao, J. Sheng, Q. Wei, M. Yan and L. Mai, *Nano Lett.*, 2014, **14**, 6250–6256.
28 J. Liu, M. Hou, Y. Shen, L. Chen, Y. Wang and Y. Xia, *Electrochim. Acta*, 2017, **241**, 179–188.
29 H.-J. Kim, K.-I. Choi, A. Pan, I.-D. Kim, H.-R. Kim, K.-M. Kim, C. W. Na, G. Cao and J.-H. Lee, *J. Mater. Chem.*, 2011, **21**, 6549–6555.
30 J. Hu, C. F. Sun, E. Gillette, Z. Gui, Y. Wang and S. B. Lee, *Nanoscale*, 2016, **8**, 12958–12969.
31 M. Y. Son, Y. J. Hong, J. K. Lee and K. Y. Chan, *Nanoscale*, 2013, **5**, 11592–11597.
32 X. Xu, P. Wu, Q. Li, W. Yang, X. Zhang, X. Wang, J. Meng, C. Niu and L. Mai, *Nano Energy*, 2018, **50**, 606–614.
33 D. W. Kim, Y. D. Ko, J. G. Park and B. K. Kim, *Angew. Chem., Int. Ed.*, 2007, **119**, 6774–6777.
34 X. Xu, C. Niu, M. Duan, X. Wang, L. Huang, J. Wang, L. Pu, W. Ren, C. Shi and J. Meng, *Nat. Commun.*, 2017, **8**, 460.
35 L. Li, S. Peng, J. Wang, Y. L. Cheah, P. Teh, Y. Ko, C. Wong and M. Srinivasan, *ACS Appl. Mater. Interfaces*, 2012, **4**, 6005–6012.
36 W. Li, D. Chen and G. Shen, *J. Mater. Chem. A*, 2015, **3**, 20673–20680.
37 O. Huei Ruey, K. Md. Maksudur Rahman, Y. Abu, H. Nor Amalina and C. Chin Kui, *RSC Adv.*, 2015, **5**, 100362–100368.
38 R. Dom, H. G. Kim and P. H. Borse, *ChemistrySelect*, 2017, **2**, 2556–2564.
39 S. Ida, K. Yamada, T. Matsunaga, H. Hagiwara, Y. Matsumoto and T. Ishihara, *J. Am. Chem. Soc.*, 2010, **132**, 17343–17345.
40 K. Sekizawa, T. Nonaka, T. Arai and T. Morikawa, *ACS Appl. Mater. Interfaces*, 2014, **6**, 10969–10973.
41 N. Sharma, K. M. Shaju, G. V. S. Rao and B. V. R. Chowdari, *J. Power Sources*, 2003, **124**, 204–212.
42 J. Chen, L. Xu, W. Li and X. Gou, *Adv. Mater.*, 2005, **17**, 582–586.
43 Y. Pan, Y. Zhang, X. Wei, C. Yuan, J. Yin, D. Cao and G. Wang, *Electrochim. Acta*, 2013, **109**, 89–94.
44 Y. Yin, W. Liu, N. Huo and S. Yang, *ACS Sustainable Chem. Eng.*, 2016, **5**, 563–570.
45 S. J. Hao, B. W. Zhang, S. Ball, J. S. Wu, M. Srinivasan and Y. Z. Huang, *J. Mater. Chem. A*, 2016, **4**, 16569–16575.
46 S. Permien, S. Indris, M. Scheuermann, U. Schurmann, V. Mereacre, A. Powell, L. Kienle and W. Bensch, *J. Mater. Chem. A*, 2014, **3**, 1549–1561.
47 M. V. Reddy, T. Yu, C. H. Sow, Z. X. Shen, C. T. Lim, G. V. Subba Rao and B. V. R. Chowdari, *Adv. Funct. Mater.*, 2010, **17**, 2792–2799.
48 J. Shim, R. Kostecki, T. Richardson, X. Song and K. A. Striebel, *J. Power Sources*, 2002, **112**, 222–230.
49 Y. Zhai, H. Mao, P. Liu, X. Ren, L. Xu and Y. Qian, *J. Mater. Chem. A*, 2015, **3**, 16142–16149.
50 X. Sun, W. Si, X. Liu, J. Deng, L. Xi, L. Liu, C. Yan and O. G. Schmidt, *Nano Energy*, 2014, **9**, 168–175.
51 Z. Wang, D. Luan, S. Madhavi, Y. Hu and X. W. Lou, *Energy Environ. Sci.*, 2012, **5**, 5252–5256.
52 G. Zhang, L. Yu, H. B. Wu, H. E. Hoster and X. W. D. Lou, *Adv. Mater.*, 2012, **24**, 4609–4613.
53 S. Laruelle, S. Grugeon, P. Poizot, M. Dollé, L. Dupont and J. M. Tarascon, *J. Electrochem. Soc.*, 2002, **149**, A627–A634.
54 W. Zeng, F. Zheng, R. Li, Y. Zhan, Y. Li and J. Liu, *Nanoscale*, 2012, **4**, 2760–2765.
55 L. Yu, Z. Wang, L. Zhang, H. B. Wu and X. W. Lou, *J. Mater. Chem. A*, 2013, **1**, 122–127.

56 J. Liu, W. Zhou, L. Lai, H. Yang, S. H. Lim, Y. Zhen, T. Yu, Z. Shen and J. Lin, *Nano Energy*, 2013, **2**, 726–732.
57 S. Mitra, P. Poizot, A. Finke and J. M. Tarascon, *Adv. Funct. Mater.*, 2010, **16**, 2281–2287.
58 X. Xu, R. Cao, S. Jeong and J. Cho, *Nano Lett.*, 2012, **12**, 4988–4991.
59 J. S. Cho, Y. J. Hong and Y. C. Kang, *ACS Nano*, 2015, **9**, 4026–4035.
60 W. Guo, W. Sun, L.-P. Lv, S. Kong and Y. Wang, *ACS Nano*, 2017, **11**, 4198–4205.
61 D. Larcher, C. Masquelier, D. Bonnin, Y. Chabre, V. Masson, J. M. Leriche and J. M. Tarascon, *J. Electrochem. Soc.*, 2003, **150**, A133–A139.
62 D. Larcher, D. Bonnin, R. Cortes, I. Rivals, L. Personnaz and J. M. Tarascon, *J. Electrochem. Soc.*, 2003, **150**, A1643–A1650.